Online supplementary of

Spatial-temporal variations of atmospheric NH_3 concentration and its dry deposition across China based on one decade of satellite and ground observations

Fan Sun[1,2], Yu Cui[1,2], Jiayin Su[3], Yifan Zhang[1,2], Xuejing Shi[1,2], Junqing Zhang[1,2], Huili Liu[1,2], Qitao Xiao[4], Xiao Lu[3], Zhao-Cheng Zeng[5], Timothy J. Griffis[6], Cheng Hu[1,2*]

[1] College of Ecology and Environment, Joint Center for sustainable Forestry in Southern China, Nanjing Forestry University, Nanjing 210037, China

[2] Yale-NUIST Center on Atmospheric Environment, Collaborative Innovation Center on Forecast and Evaluation of Meteorological Disasters (CIC-FEMD), Nanjing University of Information Science & Technology, Nanjing, 210044, China

[3] School of Atmospheric Sciences, Sun Yat-sen University, Zhuhai, 519082, China.

[4] Key Laboratory of Lake and Watershed Science for Water Security, Nanjing Institute of Geography and Limnology, Chinese Academy of Sciences

[5] School of Earth and Space Sciences, Peking University, Beijing 100871, China

[6] Department of Soil, Water, and Climate, University of Minnesota-Twin Cities, Minneapolis, MN, USA

*Corresponding author: Cheng Hu (chenghu@njfu.edu.cn or chenghu@umn.edu)

Submitted to: *Atmospheric Chemistry and Physics*

Text S1. Mann-Kendall test and Theil-Sen's slope estimator for trend analysis

The Mann-Kendall (MK) test and Theil-Sen slope estimator were employed to analyze NH_3 concentration trends. These non-parametric statistical methods have been extensively applied in meteorological and hydrological studies (Ahn et al., 2014; Yue et al., 2004), demonstrating robust performance in environmental time series analysis. The MK test represents a non-parametric approach for trend detection in temporal data that offers several analytical advantages: (1) it does not require normally distributed data, (2) it remains unaffected by missing values or outliers, and (3) it proves particularly suitable for assessing trend significance in long-term environmental datasets. The test statistic S is calculated as follows:

$$S = \sum_{i=1}^{n-1} \sum_{j=i+1}^{n} \mathrm{sgn}(x_j - x_i) \qquad (1)$$

$$\mathrm{sgn}(x_j - x_i) = \begin{cases} +1 & x_j > x_i \\ 0 & x_j = x_i \\ -1 & x_j < x_i \end{cases} \qquad (2)$$

where n denotes the sample size, x is the target variable. When n exceeds 8, the test statistic S approximately follows a normal distribution (Zhang et al., 2011). The mean (E(S)) and variance (Var(S)) of S are given by: $E(S) = 0$ (3)

$$Var(S) = \frac{n\,(n-1)\,(2n+S)}{18} \qquad (4)$$

The MK test evaluates the presence of a statistically significant monotonic trend by computing the standardized test statistic Z, calculated as follows:

$$Z = \begin{cases} \dfrac{S\text{-}1}{\sqrt{Var(S)}} & if \quad S > 0 \\ 0 & if \quad S = 0 \\ \dfrac{S+1}{\sqrt{Var(S)}} & if \quad S < 0 \end{cases} \qquad (5)$$

The standardized test statistic Z serves as an indicator of trend direction, where

positive values denote an increasing trend and negative values signify a decreasing trend. The Z-statistic further enables hypothesis testing for trend significance. In this study, we evaluated the null hypothesis (H_0) of no significant trend at a 95% confidence level ($\alpha = 0.05$).

For robust trend magnitude estimation, we employed Theil-Sen's slope estimator, a nonparametric statistical approach that determines the median slope among all possible pairwise combinations in the time series. This method offers three distinct advantages: (1) computational efficiency, (2) resistance to outliers, and (3) reliable performance with non-normally distributed data (Wang et al., 2023). Comparative studies have demonstrated that the Theil-Sen estimator outperforms ordinary least squares regression for skewed and heteroscedastic datasets, while maintaining comparable statistical performance to least squares methods for normally distributed data (Yue et al., 2004). The slope (β) is calculated as:

$$\beta = Median\left(\frac{x_j - x_i}{j - i}\right) \quad \forall\ j > i \qquad (6)$$

where xi and xj represent the sequential measurements at times i and j ($i < j$), respectively. The estimated slope β quantitatively characterizes the trend magnitude and direction: a positive β value ($\beta > 0$) indicates an increasing trend, while a negative value ($\beta < 0$) denotes a decreasing trend.

Text S2. Main land use categories and corresponding proportions in each region

The Northeast China Plain and Huang–Huai–Hai Plain are dominated by cropland. The former, is characterized by single-cropping systems (e.g., spring wheat and maize), with cropland accounting for 46.28% of the area. The Huang–Huai–Hai Plain, a major agricultural region, is characterized by double- or triple-cropping systems (e.g., winter wheat and cotton), and has a higher cropland proportion of 57.15%. Subregions such as the Yunnan–Guizhou Plateau, Southern China, Sichuan Basin and Surrounding Areas, Middle–Lower Yangtze Plain, and Loess Plateau are primarily forested. These regions encompass China's three major natural forest areas, particularly in the southwest and south. Forest cover proportions in these regions are 68.48%, 70.60%, 43.01%, 47.26%, and 37.63%, respectively. The Northern Arid and Semi-Arid Region includes the Taklamakan Desert and is primarily characterized by bare land (47.58%). The Qinghai–Tibet Plateau features extensive alpine meadows and grasslands, with grassland accounting for 70.47% of its land surface.

Text S3. Details of six emission inventories

The Inversed Emission Inventory for Chinese Air Quality (CAQIEI), jointly developed by the Institute of Atmospheric Physics, Chinese Academy of Sciences (IAP, CAS), and the China National Environmental Monitoring Center (CNEMC), is a top-down long-term emission inventory for China. It provides emissions data for multiple air pollutants—including SO_2 and NO_x—from 2013 to 2020, with a horizontal resolution of 15 km. CAQIEI has been shown to effectively reduce biases in *prior* emission inventories (Kong et al., 2023).

The Multi-resolution Emission Inventory for China (MEIC), developed by Tsinghua University, is a bottom-up emission inventory model that covers the period from 1990 to 2020. It offers spatially resolved emission data at provincial scale and in grid formats using geographic projections (0.25°, 0.5°, and 1.0° latitude/longitude) and Lambert conformal conic projection. In this study, provincial-level data from MEIC were utilized to calculate and analyze long-term emission trends of SO_2, NOx, and NH_3 across China (Zheng et al., 2018).

The Air Benefit and Cost and Attainment Assessment System - Emission Inventory version 2.0 (ABaCAS), co-developed by Tsinghua University, South China University of Technology, and other institutions, is a decision-support system for cost-effectiveness evaluation of air pollution control and attainment planning. The dataset spans from 2005 and has been updated through 2021, with spatial resolutions including provincial scale and a 27 km grid (Li et al., 2023).

The Community Emissions Data System (CEDS) is a global emission inventory that provides gridded emissions of various gases and aerosol precursors—including CO_2, CH_4, NO_x, and SO_2—with spatial resolutions of 0.5° and 0.1°. The dataset spans from 1750 to the present, with most post-1950 data being the result of extensive harmonization and processing (McDuffie et al., 2020).

The Emissions Database for Global Atmospheric Research (EDGAR), developed by the Joint Research Centre (JRC) of the European Union, provides global gridded emissions at a 0.1° resolution as well as national totals from 1970 to 2022. The database includes annual, monthly, and hourly emission data for a wide range of pollutants (Crippa et al., 2024).

The Dynamic Projection model for Emissions in China (DPEC), developed by Tsinghua University, is a forward-looking model that projects China's future emissions under multiple scenarios. The current version of the DPEC dataset (v1.2) includes five policy scenarios: early peak–net zero–clean air, on-time peak–net zero–clean air, on-time peak–clean air, clean air, and baseline. The spatial resolution is consistent with that of the MEIC inventory (Cheng et al., 2023)

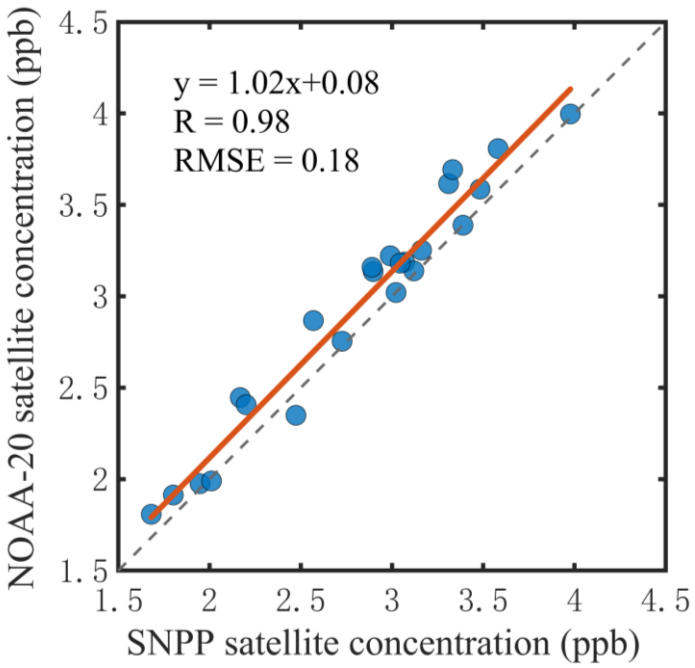

Figure S1. Comparisons of monthly mean atmospheric NH_3 concentrations derived from two satellite observations during the overlap period 2019-2021 (Units: ppb)

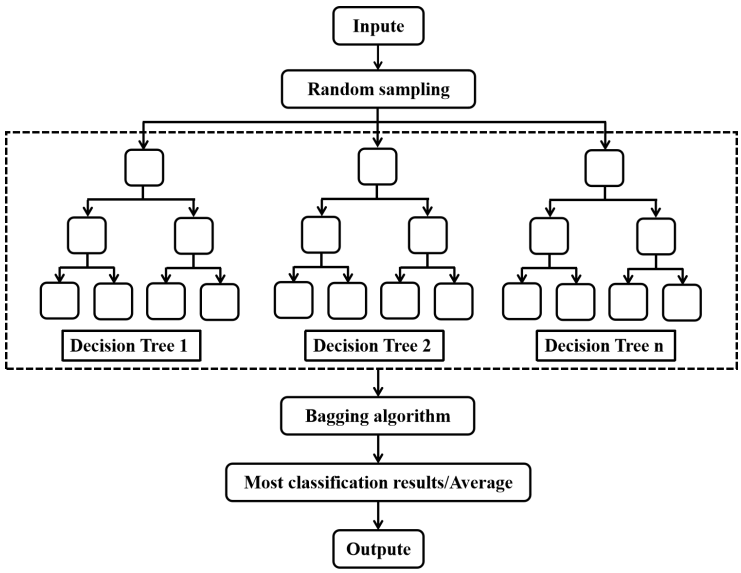

Figure S2. Schematic illustration of the random forest (RF) algorithm architecture.

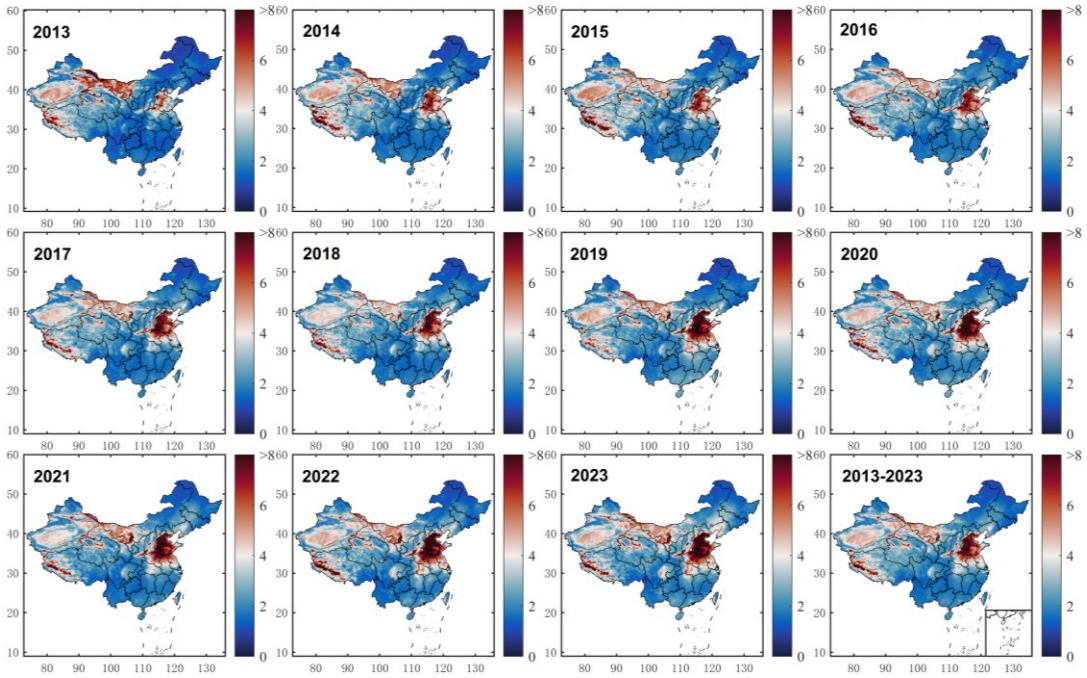

Figure S3. The spatial distribution of annual averaged NH_3 concentration from 2013 to 2023 (Units: ppb).

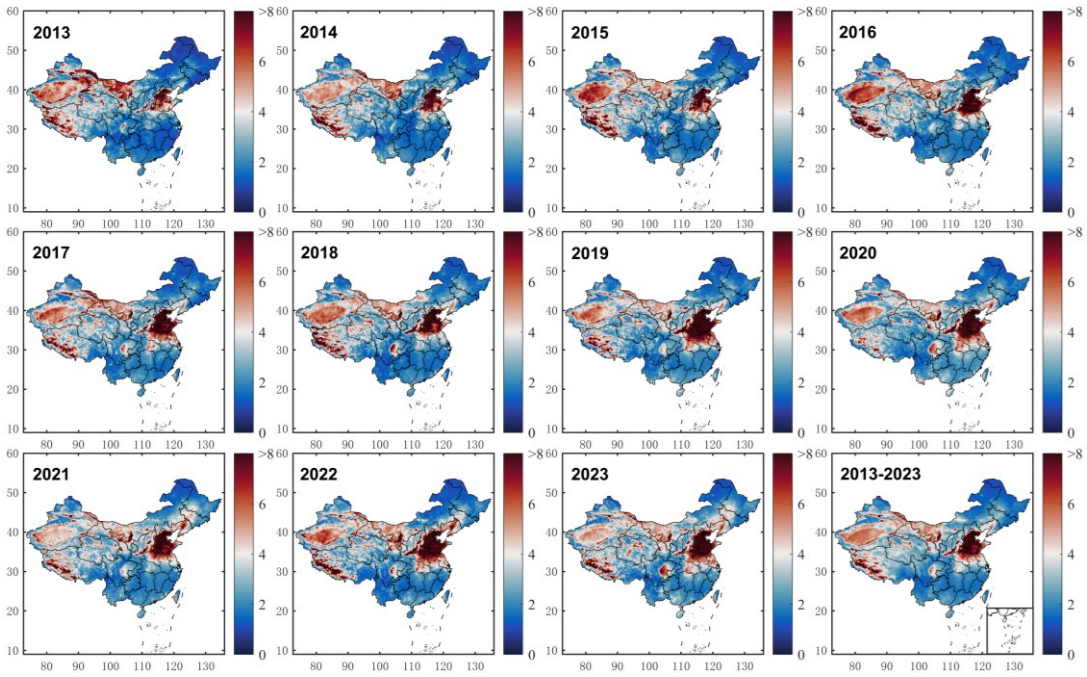

Figure S4. The spatial distribution of Spring time averaged NH_3 concentration from 2013 to 2023 (Units: ppb).

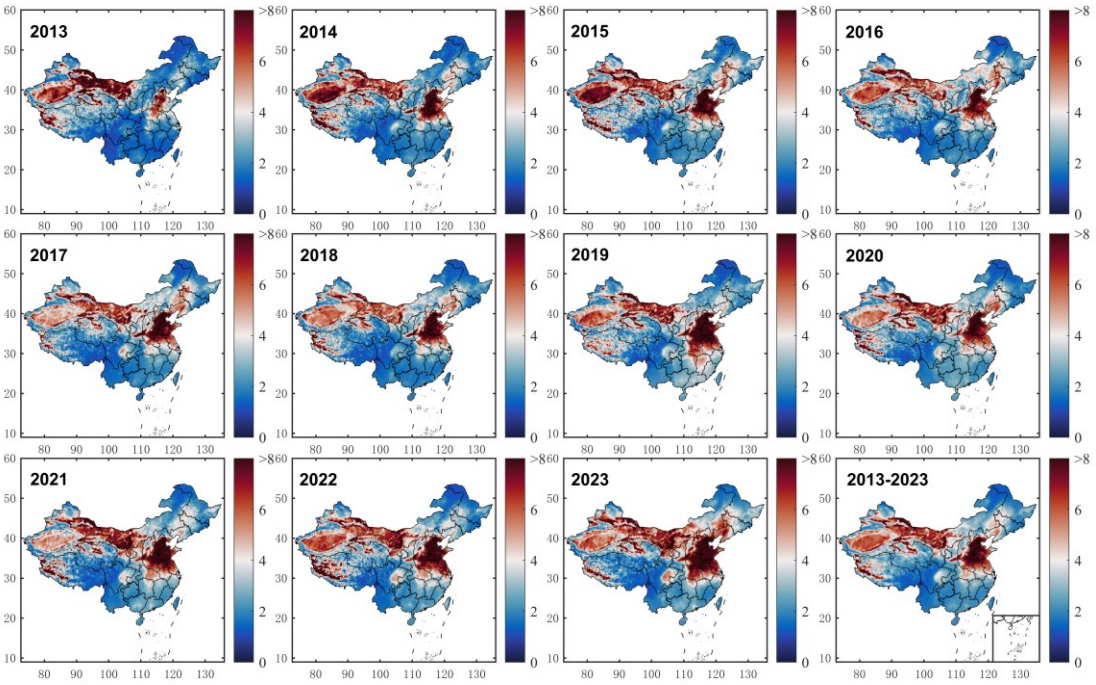

Figure S5. The spatial distribution of Summer time averaged NH_3 concentration from 2013 to 2023 (Units: ppb).

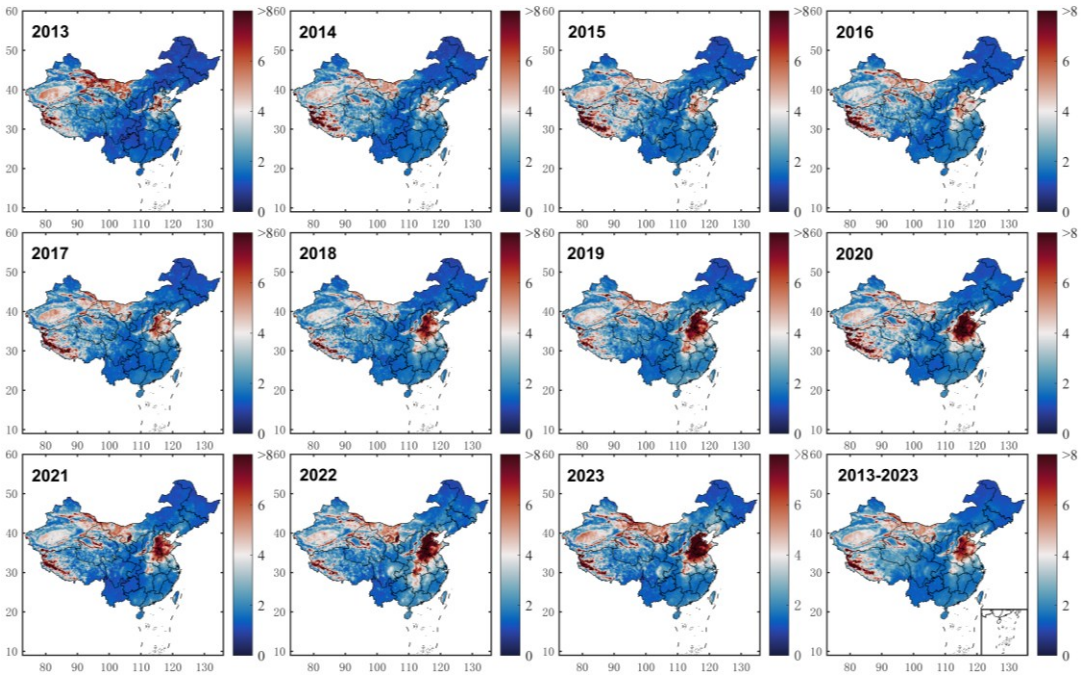

Figure S6. The spatial distribution of Autumn time averaged NH_3 concentration from 2013 to 2023 (Units: ppb).

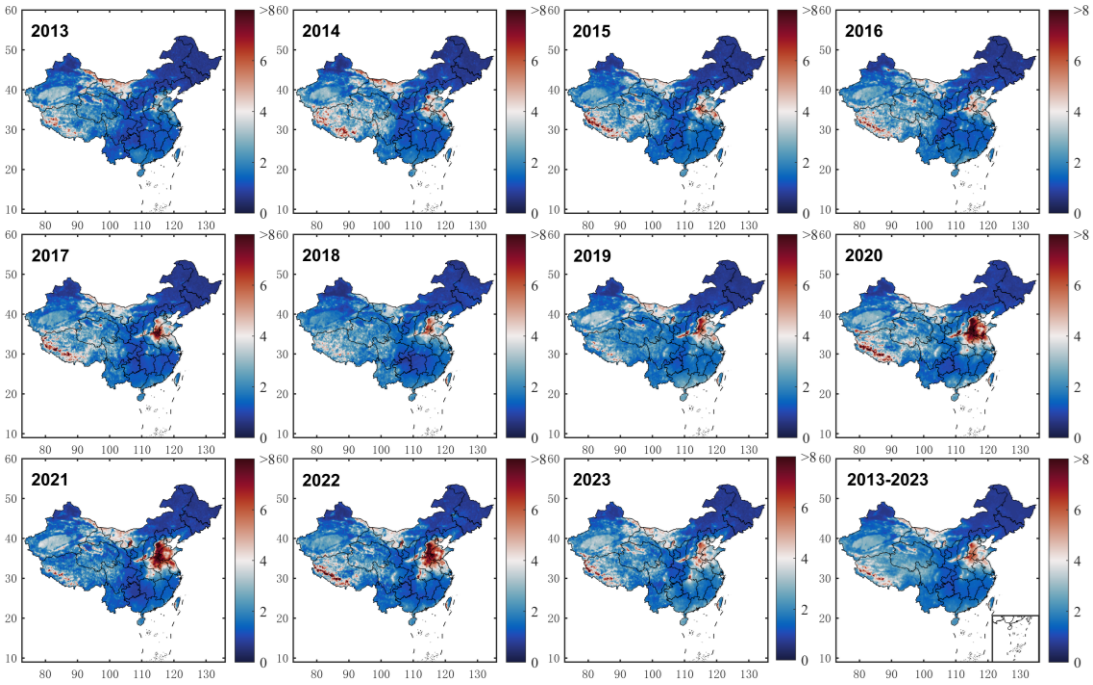

Figure S7. The spatial distribution of Winter time averaged NH_3 concentration from 2013 to 2023 (Units: ppb).

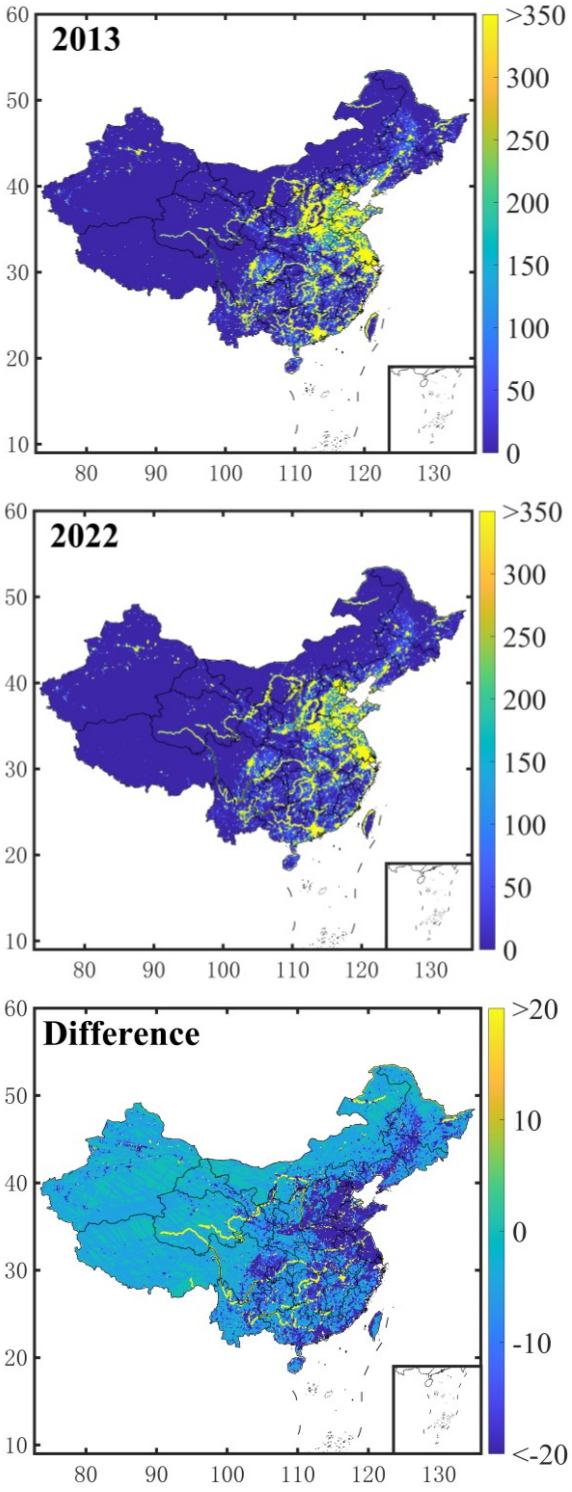

Figure S8. The spatial distribution of SO_2 emissions and their differences in 2013 and 2022 (Units: t).

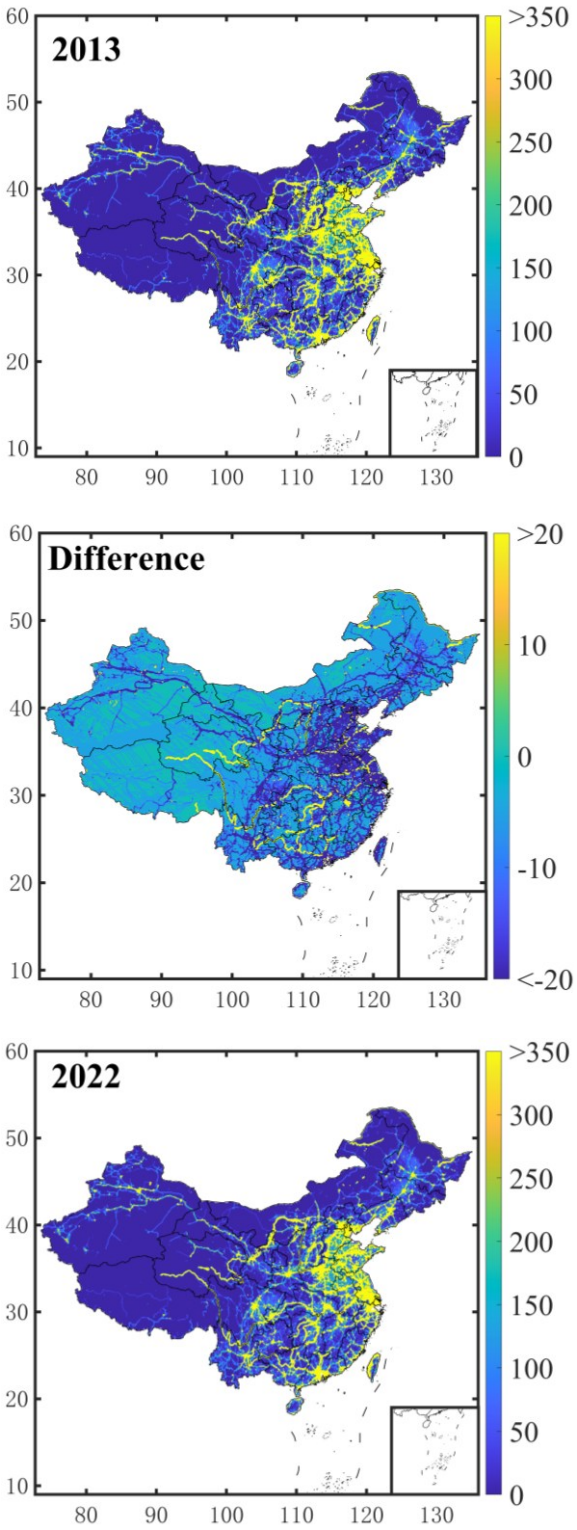

Figure S9. The spatial distribution of NOx emissions and their differences in 2013 and 2022 (Units: t).

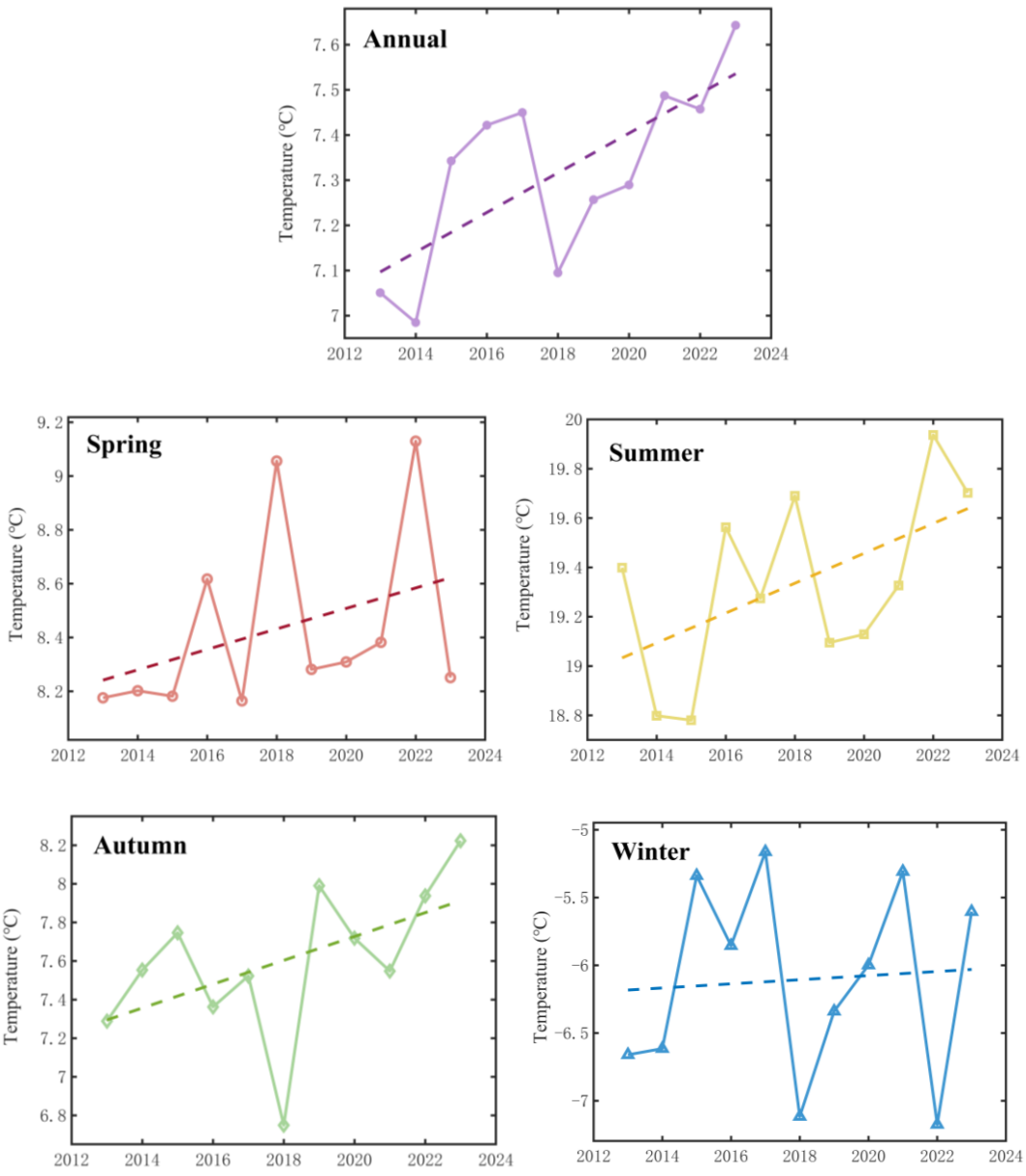

Figure S10. Annual averaged and seasonal temperature variations from 2013 to 2023.

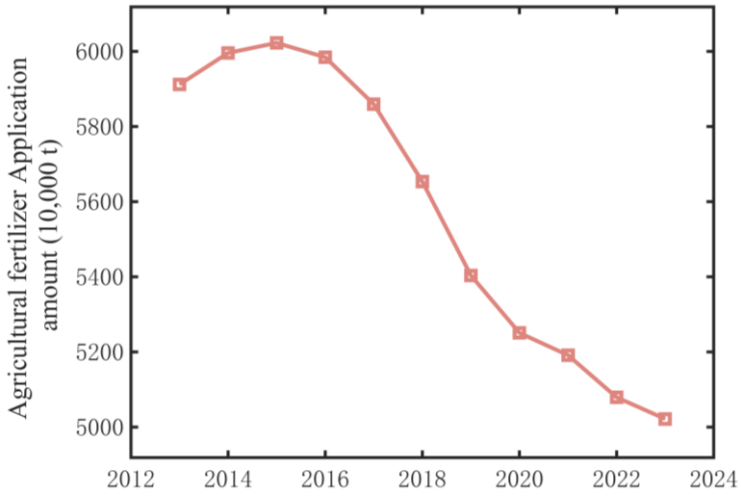

Figure S11. The annual amount of agricultural fertilizer usage for China from 2013 to 2023 (Units: million metric tons).

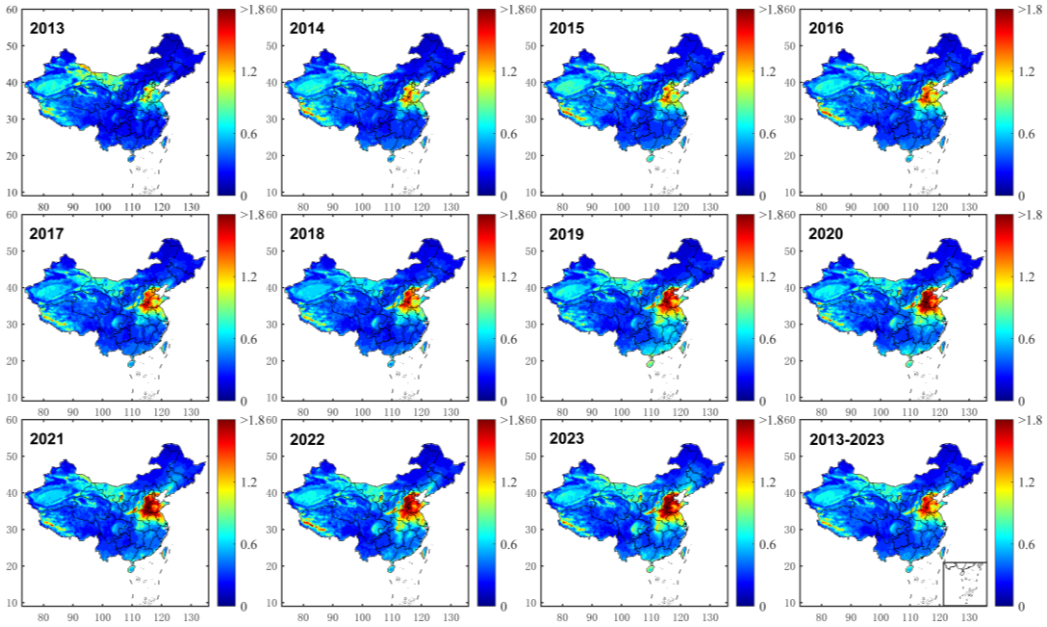

Figure S12. The spatial distribution of annual dry deposition of NH_3 from 2013 to 2022 (Units: g m^{-2})

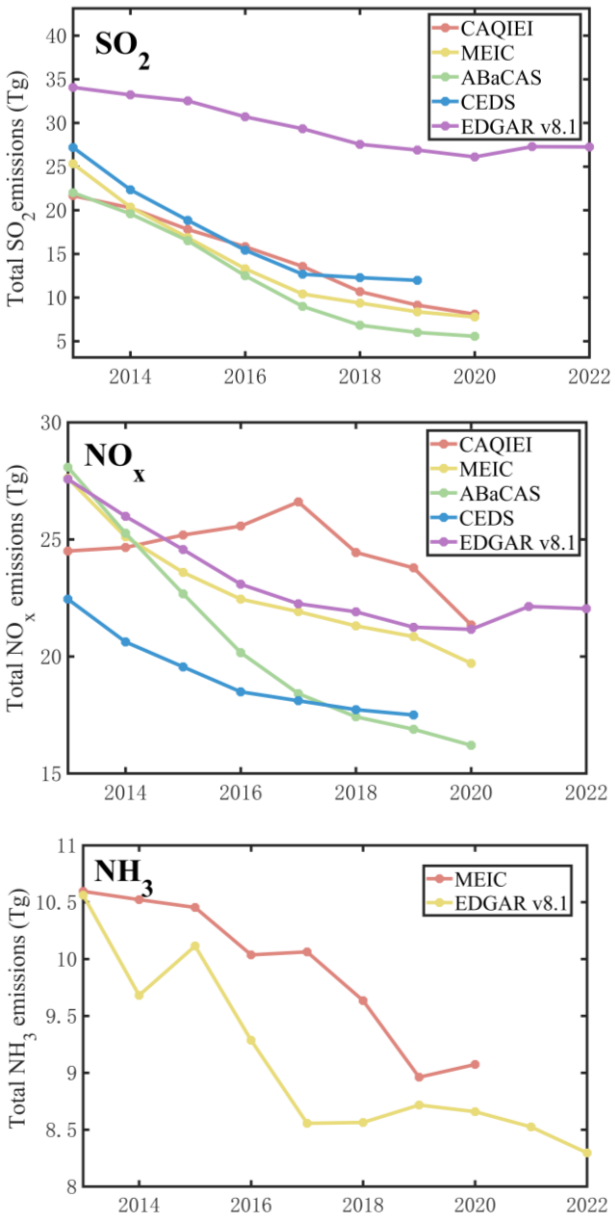

Figure S13. Time series of annual emissions of SO_2, NO_x and NH_3 over China from 2013 to 2022 obtained from EDGAR v8.1 and previous inventories.

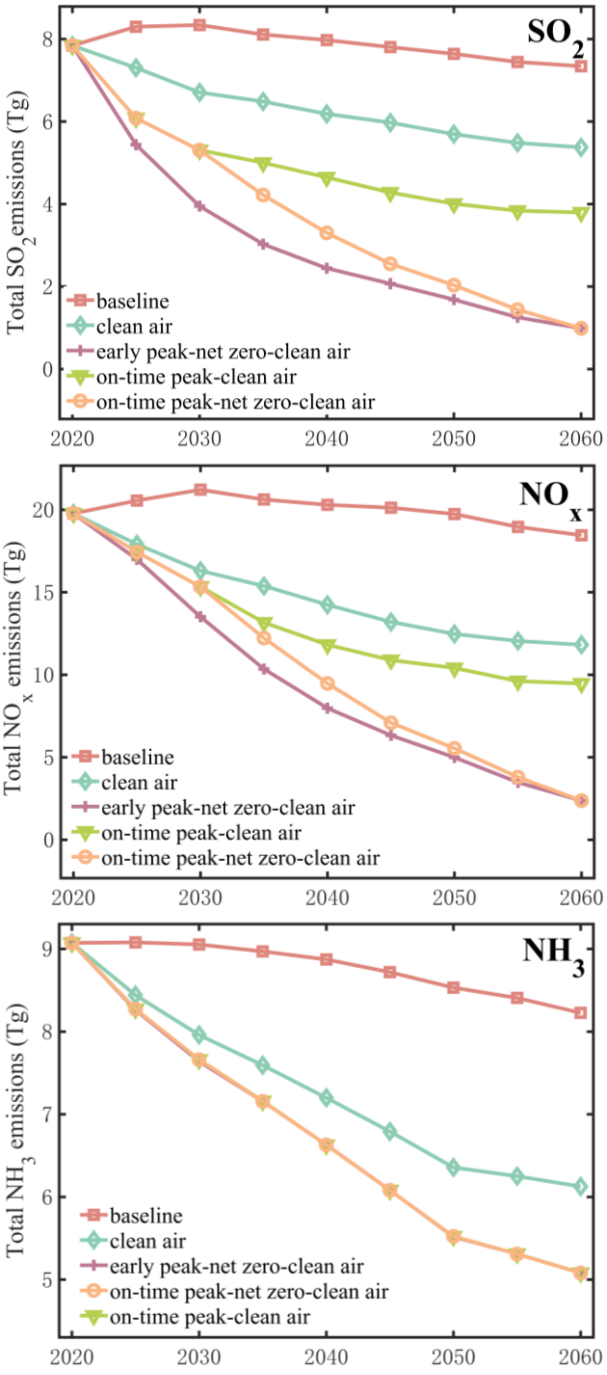

Figure S14. Projected emission trends of SO_2, NO_x, and NH_3 under five future scenarios.

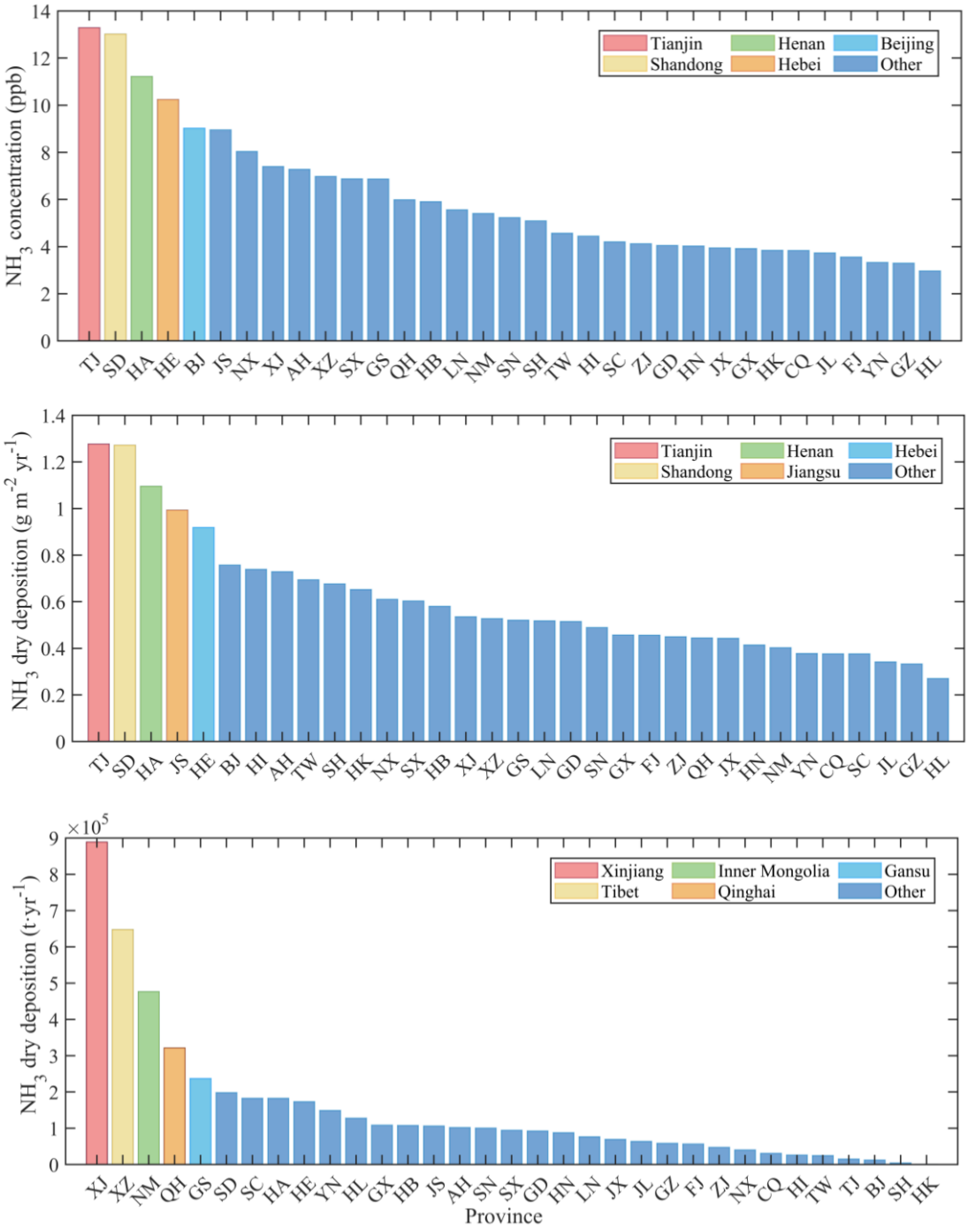

Figure S15. (a) Annual NH_3 concentration (Units: ppb); (b) Annual mean area-specific dry deposition flux of NH_3 (g m^{-2} yr^{-1}); (c) annual total dry deposition of NH_3 (t yr^{-1}) for different provinces of averages over 2013-2023.

425 **Table S1.** The details of different agricultural zoning and corresponding provinces

Agricultural zoning	Include provinces
Northeast China Plain	Heilongjiang; Jilin; Liaoning
Yunnan-Guizhou Plateau	Yunnan; Guizhou; Guangxi
Northern arid and semiarid region	Xinjiang; Gansu; Inner Mongoria; Ningxia
Southern China	Guangdong; Fujian; Hainan; Taiwan
Sichuan Basin and surrounding regions	Sichuan; Chongqing
Middle-lower Yangtze Plain	Jiangsu; Zhejiang; Anhui; Hubei; Hunan; Jiangxi
Qinghai Tibet Plateau	Tibet; Qinghai
Loess Plateau	Shanxi; Shaanxi
Huang-Huai-Hai Plain	Shandong; Hebei; Henan; Beijing; Tianjing

426
427
428
429
430
431
432
433
434
435
436
437
438
439
440
441
442
443
444
445
446
447
448
449
450
451

452 **Table S2.** Detailed information of 6 different NH3 emission inventories.

Data	Domain	Major institutions	Version	Time period	Spatial resolution	References
CAQIEI	China	IAP, CAS; CNEMC	v1.0	2013-2020	15 km	Kong et al., 2023
MEIC	China	Tsinghua University	v1.4	1990-2020	0.25° 0.5° 1.0° Province	Zheng et al., 2018
ABaCAS	China	Tsinghua University	v2.0	2005-2021	Province 27 km	Li et al., 2023
CEDS	Global	Harvard University; NASA; EPA	v2024_04_01	1750-2023	0.5° 0.1°	McDuffie et al., 2020
EDGAR	Global	JRC	V8.1	1970-2022	0.1°	Crippa et al., 2024
DPEC	China	Tsinghua University	v1.2	2020; 2025; 2030; 2035; 2040; 2045; 2050; 2055; 2060	0.25° 0.5° 1.0° Province	Cheng et al., 2023

Table S3. Annual growth rates of NH_3 concentration, dry deposition velocity, area-specific dry deposition flux, and total deposition across different underlying surface types

Type	Annual growth in NH_3 concentration (ppb yr^{-1})	Annual growth of NH_3 dry deposition velocity (cm s^{-2} yr^{-1})	Annual growth of NH_3 dry deposition flux (g m^{-2} yr^{-1})	Annual growth amount of total NH_3 dry deposition (t yr^{-1})
City	0.39	0.0013	0.04	1.3682e+04
Cropland	0.28	0.0012	0.03	5.2324e+04
Forest	0.11	8.0342e-04	0.01	3.1404e+04
Grassland	0.03	-5.5254e-05	0.00	5.8843e+03
China	0.10	4.2563e-04	0.01	9.7757e+04

Table S4. Relative changes in NH_3 concentrations and dry deposition velocities by underlying surface type and national aggregates

Type	Contribution percentage of NH_3 concentration variation	Contribution percentage of NH_3 dry deposition velocity variation
City	72.6%	27.4%
Cropland	75.8%	24.2%
Forest	81.2%	18.8%
Grassland	80.3%	19.7%
China	80.3%	19.7%

References:

Ahn K H, Merwade V. Quantifying the relative impact of climate and human activities on streamflow. Journal of Hydrology, 2014, 515: 257-266.

Cheng J, Tong D, Liu Y, et al. A synergistic approach to air pollution control and carbon neutrality in China can avoid millions of premature deaths annually by 2060. One Earth, 2023, 6(8): 978-989.

Crippa M, Guizzardi D, Pagani F, et al. Insights into the spatial distribution of global, national, and subnational greenhouse gas emissions in the Emissions Database for Global Atmospheric Research (EDGAR v8.0). Earth System Science Data, 2024, 16(6): 2811-2830.

Kong L, Tang X, Wang Z, et al. Changes of air pollutant emissions in China during two clean air action periods derived from the newly developed Inversed Emission Inventory for Chinese Air Quality (CAQIEI). Earth System Science Data Discussions, 2023, 2023: 1-47.

Li S, Wang S, Wu Q, et al. Emission trends of air pollutants and CO_2 in China from 2005 to 2021. Earth System Science Data, 2023, 15(6): 2279-2294.

McDuffie E E, Smith S J, O'Rourke P, et al. A global anthropogenic emission inventory of atmospheric pollutants from sector-and fuel-specific sources (1970–2017): an application of the Community Emissions Data System (CEDS). Earth System Science Data Discussions, 2020, 2020: 1-49.

Wang R, Pan D, Guo X, et al. Bridging the spatial gaps of the Ammonia Monitoring Network using satellite ammonia measurements. Atmospheric Chemistry and Physics, 2023, 23(20): 13217-13234.

Yue S, Wang C Y. The Mann-Kendall test modified by effective sample size to detect trend in serially correlated hydrological series. Water resources management, 2004, 18(3): 201-218.

Zhang Q, Li J, David Chen Y, et al. Observed changes of temperature extremes during 1960–2005 in China: natural or human-induced variations?. Theoretical and Applied Climatology, 2011, 106: 417-431.

Zheng B, Tong D, Li M, et al. Trends in China's anthropogenic emissions since 2010 as the consequence of clean air actions. Atmospheric Chemistry and Physics, 2018, 18(19): 14095-14111.